Journal of
Applied Physics

# Implementation of Talbot–Lau x-ray deflectometry in the pulsed power environment using a copper X-pinch backlighter

Cite as: J. Appl. Phys. **127**, 203301 (2020); https://doi.org/10.1063/5.0001910
Submitted: 21 January 2020 . Accepted: 07 May 2020 . Published Online: 22 May 2020

**Milenko Vescovi, Maria Pia Valdivia, Felipe Veloso, et al.**

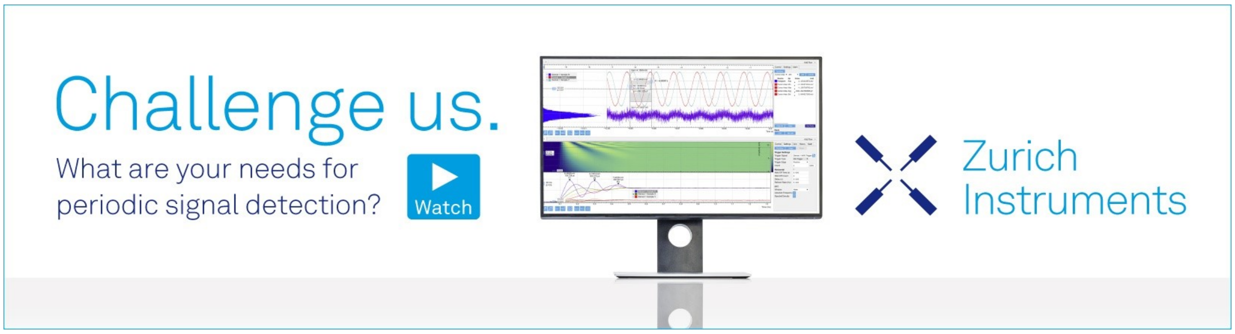

AIP Publishing

Journal of Applied Physics ARTICLE scitation.org/journal/jap

# Implementation of Talbot–Lau x-ray deflectometry in the pulsed power environment using a copper X-pinch backlighter

Cite as: J. Appl. Phys. **127**, 203301 (2020); doi: 10.1063/5.0001910
Submitted: 21 January 2020 · Accepted: 7 May 2020 ·
Published Online: 22 May 2020

Milenko Vescovi,[1] Maria Pia Valdivia,[2] Felipe Veloso,[1,a)] Dan Stutman,[2] and Mario Favre[1]

**AFFILIATIONS**

[1] Instituto de Física, Pontificia Universidad Católica de Chile, Casilla 306, Santiago, Chile
[2] Department of Physics and Astronomy, Johns Hopkins University, Baltimore, Maryland 21218, USA

[a)] **Author to whom correspondence should be addressed:** fveloso@fis.uc.cl

## ABSTRACT

A Talbot–Lau x-ray deflectometer can map electron density gradients in high energy density plasmas, as well as provide information about plasma elemental composition through single-image x-ray refraction and attenuation measurements. A new adaptation to a pulsed power environment used backlighting from copper X-pinches, allowing for electron density mapping of a low-Z object. Even though the X-pinch backlighter is not properly optimized for emitting x-rays in terms of source size and photon fluence, Moire fringe patterns with contrast up to 14% and fringe shift due to refraction on a beryllium object are obtained. Due to the proximity of the deflectometer with the X-pinch (~6 cm), it is shown that a protective filter is required to avoid damage in the closest (i.e., source) grating due to both plasma debris and mechanical shock. Regarding grating survival, these did not show any damage due to the intense magnetic field or heating induced by plasma radiation. Electron density on beryllium was measured with a difference lower than 16%. The areal electron density mapping of the sample was limited by source size characteristics, in similarity to transmission radiography. These results show the potential of plasma electron density as well as material mapping through Talbot–Lau x-ray deflectometry in a pulsed power environment.

## I. INTRODUCTION

A Talbot interferometer can measure light source angular deviations caused by refraction index gradients[1] and through phase-contrast methods, and it can effectively retrieve and map electron density gradients in matter.[2] When used in the Talbot–Lau X-ray Deflectometry (TXD) configuration, two gratings with a small rotation between them generate a Moiré fringe pattern. These fringes enable single shot imaging, in contrast to the phase-stepping methods used in medical Talbot–Lau interferometry.[3] Additionally, a third micro periodic grating allows the use of the diagnostic with spatially incoherent backlighting sources. Considering that standard visible light interferometry is limited by critical density[4] and that refraction angles scale with energy as ~1/E$^2$, lower probing energies provide better interferometer sensitivity. Therefore, x-ray diagnostics are necessary to detect higher densities in higher density plasmas. Moreover, in radiography, the refraction signatures for objects probed with 1–100 keV energies are more sensitive than the attenuation signatures in low Z-materials.[5,6] This fact can be seen when comparing the ratio β/δ for different materials (where β and δ are the coefficients of the complex refractive index $n = 1 - \delta - i\beta$). For instance, in the case of 30 keV photons, $\beta/\delta \sim 10^{-5}$ in beryllium ($Z = 4$), $\beta/\delta \sim 10^{-3}$ in calcium ($Z = 20$), and $\beta/\delta \sim 10^{-2}$ in tungsten ($Z = 74$)[32] Thus, TXD can provide a wealth of information about plasmas in the high energy density regime not currently available through transmission-based radiography.

High Energy Density (HED) experiments are mostly performed using either high power lasers to ablate solid targets or pulsed high current drivers to produce dense transient z-pinch plasmas in HED regimes.[8,24,37–39] Recently, a Talbot–Lau deflectometer was adapted to work on a High Energy Density (HED) facility.[6] In that adaptation, a thin copper foil was illuminated by an ~29 J, 8 ps laser pulse produced K-shell emission at 8 keV. The electron density of a static low-Z object was retrieved from a Moiré image and mapped through TXD. Nonetheless, that particular deflectometer does not necessarily comply with the requirements for its use in pulsed power environments where intense magnetic fields and debris from both plasma and electrodes together with a high harsh electrically noisy environment are present. A Talbot–Lau x-ray deflectometer adaptation for a pulsed power environment will extend TXD capabilities as HED diagnostic by making it available to a wider variety of plasma experiments. Therefore, we describe the adaptation of the Talbot–Lau deflectometer to operate using an x-pinch backlighter in a pulsed power environment. The new TXD adaptation provided a micrometer-sized nanosecond x-ray emission source. The source originated from a single hotspot located at the x-pinch cross point.[7] Moreover, the adaptation will provide complimentary information to that currently provided by standard pulsed power diagnostics. For example, magnetized liner inertial fusion experiments[8] could benefit from TXD diagnostic characterization. TXD could deliver reliable electron density, mixing, and micro-instability information. Moreover, since x-ray backlighters can penetrate thin liners and wires, TXD can provide additional and complementary information to that available through standard visible laser interferometry[9] before ablation begins as well as during highly dense plasma formation.

X-pinch discharge dynamics have been widely studied for over three decades.[10,11] In particular, the full current flows at the cross point so that a localized hotspot is formed when full compression is achieved. This compression results in radiation emission in the form of K-shell point sources[12–14] and lower energy free-bound continuum. Temporal emission characteristics and source size are dependent on current, the x-pinch material, and the plasma temperature achieved,[15] which implies that the optimal X-pinch source for a given pulsed power driver depends on driver and load parameters. X-ray emission from x-pinches has been used in many applications. Due to their good temporal (a few ns or lower) and spatial (a few to tens of $\mu$m) resolution, they make good backlighters[16,17] and are often used in x-ray radiography,[18,19] metrology,[20,21] lithography,[22] x-ray Thomson scattering,[23] etc. In particular, the use of standard ~1–20 keV backlighters in TXD will allow for high contrast imaging of low to mid-Z plasmas generated from wires or foils driven by pulsed power generators.

## II. TXD: PULSED POWER ENVIRONMENT ADAPTATION

The Talbot–Lau interferometer (shown in Fig. 1), composed of three micro-periodic gratings, had a design energy that maximizes the fringe contrast for photons of 8 keV. This design is chosen so there would be no overlap between the backlighter and the expected plasma self-emission energies,[24] which ensures accurate electron density profile retrieval even in the presence of background plasma radiation. The grating substrates were deposited over 10 $\mu$m thick polyimide membranes. The source grating ($g_0$) has a 2.4 $\mu$m period and a gold bar height of 24 $\mu$m. The phase grating ($g_1$) has a 4.0 $\mu$m period and a nickel bar height of 3.0 $\mu$m. The analyzer grating ($g_2$) has a period of 12 $\mu$m and a 24 $\mu$m gold bar height. The gratings have been used in previous configurations.[9] The source grating is protected from both the x-pinch radiation and debris by using either an 11 $\mu$m aluminum filter or a 14 $\mu$m copper filter. A beryllium sheet of $1 \times 1$ cm$^2$, 0.5 mm thickness, is probed edge-on and rotated at about 3°. This object is placed at ~0.5 cm behind the phase grating rotation stage, hence giving the deflectometer an angular sensitivity of ~210 $\mu$rad. This angular sensitivity has been calculated following the procedures described in Refs. 9 and 34–36 In contrast to laser experiments, in a pulsed power environment, it is not recommendable to use digital x-ray cameras given the high electrical noise produced by several different spark discharges common in the operation of pulsed power drivers. For this reason, the Moiré images were recorded using Carestream D-Speed x-ray film instead. The films were filtered with aluminum foil (22 $\mu$m) and placed behind the analyzer grating rotation stage with an object magnification of ~2. The general TXD pulsed power setup is shown below in Fig. 1.

Due to the limited size of the vacuum chamber where the experiments took place, the interferometer was set in the first Talbot order (m = 1), with an ~10 cm total length. The Talbot order, which is inversely proportional to the energy bandwidth[31,] sets the maximum contrast possible for a determined energy. A contrast curve obtained with the XWFP code[25] is shown in Fig. 2, along with filter transmission and copper x-ray characteristic lines expected from the pulsed power x-ray source.

The Talbot–Lau interferometer is illuminated with x-ray pulses emitted by double copper x-pinch loads ($4 \times 25\,\mu$m diameter wires). The x-pinch loads are driven by the Llampudken generator[26] capable of delivering 350 kA, an ~350 ns rise time. Two 0.25 $\mu$F Marx capacitor banks were charged up to 240 kV to deliver ~7 kJ energy to the load with an equivalent impedance of 0.8 Ω. The x-pinch is loaded in the middle of the vacuum chamber so that radiation emission is expected to be isotropic for all radial diagnostic ports. As previously discussed, the optimal x-ray source for an X-pinch depends on several load and generator parameters, so it is possible that the chosen load is not the optimal for producing the smallest (and/or brightest) backlight source. A further study on finding the optimal X-pinch source for ~8 keV photons given our generator parameters is beyond the scope of this paper. The Talbot–Lau interferometer platform is placed along the line of sight of one of the ports, with the source grating ~6 cm away from the load and aligned with the x-pinch cross point.

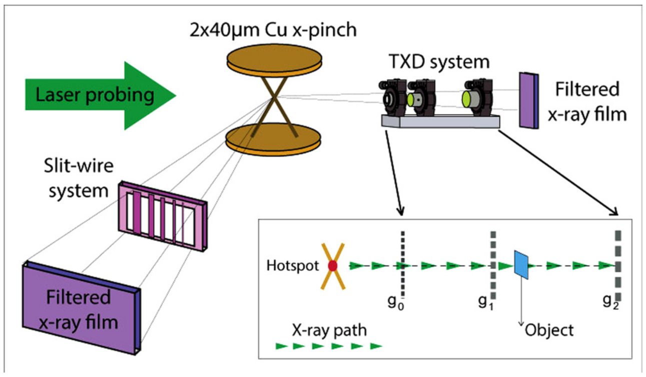

**FIG. 1.** X-pinch x-ray backlighter schematic of the Talbot–Lau system and additional diagnostics.

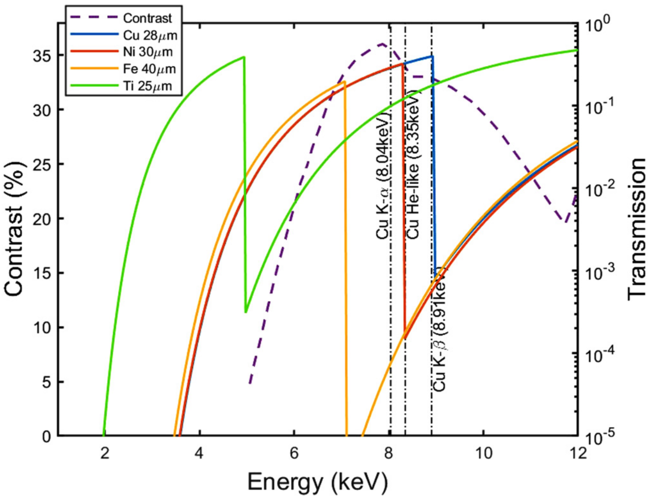

**FIG. 2.** Filter transmission curves, together with a contrast curve for the Talbot–Lau interferometer for first (m = 1) order. Cu-Kα, Cu-Kβ, and Cu-He-like lines are also indicated.

In order to monitor the x-ray emission from the X-pinch, three cross-calibrated x-ray AXUV diodes[33] (labeled as A, B, and C) delivered emission timing information with ∼1 ns resolution. Ross-pair filtration was provided using 28 $\mu$m Cu on diode A, 30 $\mu$m Ni for diode B, and 40 $\mu$m Fe for diode C. This filter combination gave us spectral information by distinguishing different energy ranges. Particular attention was provided to the Cu-Kα, Cu-Kβ, and Cu-He-like emissions in the 8–9 keV range where the deflectometer contrast is maximized. Both transmission curves and deflectometer contrast are shown in Fig. 2. A similarly filtered set of slit wires[27] provided one-dimensional imaging which allowed source size quantification for the different emission lines. A single slit of ∼30 $\mu$m size was placed 5.8 cm away from the x-pinch. The slit was filtered with 15 $\mu$m Ni, 14 $\mu$m Cu, 20 $\mu$m Fe, and 25 $\mu$m Ti. The filters were independent of the slit entrance (i.e., not stacked) and each one of them used two different W wire diameters (750 $\mu$m and 500 $\mu$m). It is worth noting that some of these filters provided similar information to the Ross-pair AXUV diodes (and, therefore, the filter transmission can also be obtained from Fig. 2). The slit-wire images were recorded with Carestream D-Speed x-ray film and a magnification of ∼0.9×.

## III. X-PINCH BACKLIGHTING AND TXD PERFORMANCE

The x-ray emission from an X-pinch comes from two main source mechanisms. First, emission is produced by the compression of the central crossing point of the configuration, producing an ∼$\mu$m size hotspot. A secondary emission is related to the formation of a mini-diode gap that accelerates electrons whose interaction with the surrounding plasma produces ∼10s–100s $\mu$m size bright emitting x-ray sources. The energy range of photons produced by the first pulse is mostly on the ∼keV range, whereas the second source has higher photon energies produced by bremsstrahlung (∼10 s keV).[14] When optimizing an X-pinch load for a particular current driver, the predominant source can be selected.[14,15] The monitoring of the X-pinch dynamics can provide information to elucidate which mechanism is associated to a particular emission in both time and position. In order to monitor the x-pinch dynamics, the self-emission of the plasma in the XUV-UV range is obtained using pinhole imaging. Time-resolved images are shown in Fig. 3(a) which are provided by 150 $\mu$m and 60 $\mu$m pinhole diameters and recorded onto microchannel-plates (MCPs) with a gating pulse of ∼5 ns. According to the positioning of pinholes (at 23 cm from the plasma) and MCP recording plate (at 34 cm from the plasma), the spatial resolutions are 220 $\mu$m and 90 $\mu$m for the 150 $\mu$m and 60 $\mu$m pinhole diameters, respectively. These limits of resolution are given by geometrical effects.[28] Additionally, time-integrated images are recorded using open-shutter film exposure using Carestream D-speed x-ray film as the detector. These images use three 100 $\mu$m diameter pinholes filtered with 21 $\mu$m Cu, 25 $\mu$m Ti, and 2 $\mu$m Al, respectively. The magnification of this second set of pinholes is M ∼ 0.4. Figure 3 shows self-emission images of the

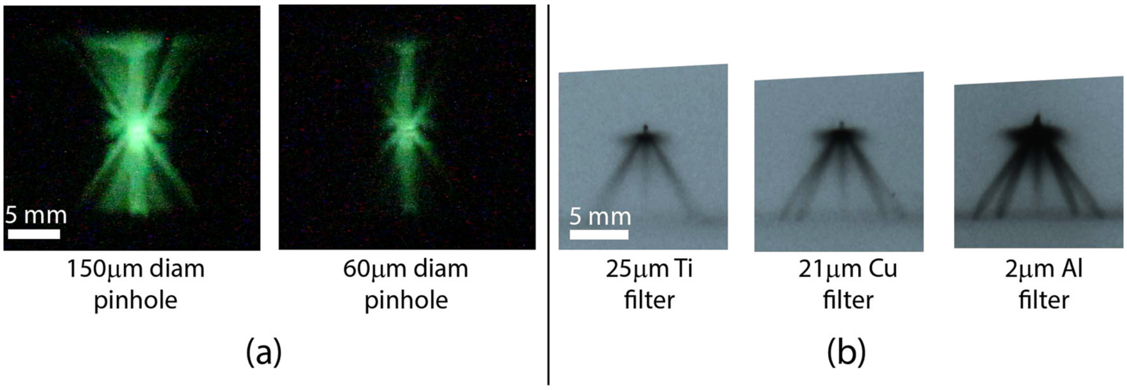

**FIG. 3.** (a) Simultaneous time-resolved MCP images using different pinhole diameters. (b) Time-integrated pinhole images using different filters. In all images, the cathode is on top, and the anode is at the bottom.

plasma with these diagnostics. In Fig. 3(a), the formation of a diode gap at the crossing point of the wires can be observed. In addition, Fig. 3(b) shows x-ray emission from the initial position of the copper wires and the axial jet on the anode half of the x-pinch load. The vertical asymmetry of this source suggests the presence of accelerated electrons propagating through the plasma toward the anode. Besides this, in time-integrated images filtered with Ti and Cu, a bright-round source is seen at the crossing point position which corresponds to the geometrical projection of the pinhole to the film.

The temporal characteristics of the x-ray emission are shown in Fig. 4 for two different shots. As discussed in Sec. I, the performance of X-pinches strongly depends on the driving current. Even though in the shots presented in Fig. 4 the current driving the plasma differs substantially (and, therefore, the x-ray emission as well), both shots produce a Talbot–Lau fringe pattern. This demonstrates the robustness of the diagnostic in a pulsed power environment. Figure 4(a) shows a well-pronounced x-ray peak, ~5 ns FWHM is obtained at t ~ 310 ns. In addition, the AXUV diodes record different amplitudes of the signals due to their differences on their filtering. It can be observed that the peak on the diode labeled "B" is five times higher than that on the "C" diode. According to the filter transmission shown in Fig. 2, the emission at t ~ 310 ns has an important contribution from the Cu-Kα line. Using diode sensitivity and cross-calibration of the diodes, this Cu-Kα emission yield is roughly ~1.0 mJ (on this shot). Furthermore, Fig. 5 shows time-integrated slit-wire images of the shot of Fig. 4(b). In this figure, two horizontal lines are observed with different intensities which indicate two sources, roughly separated by ~0.3 mm between them, in the vertical direction.

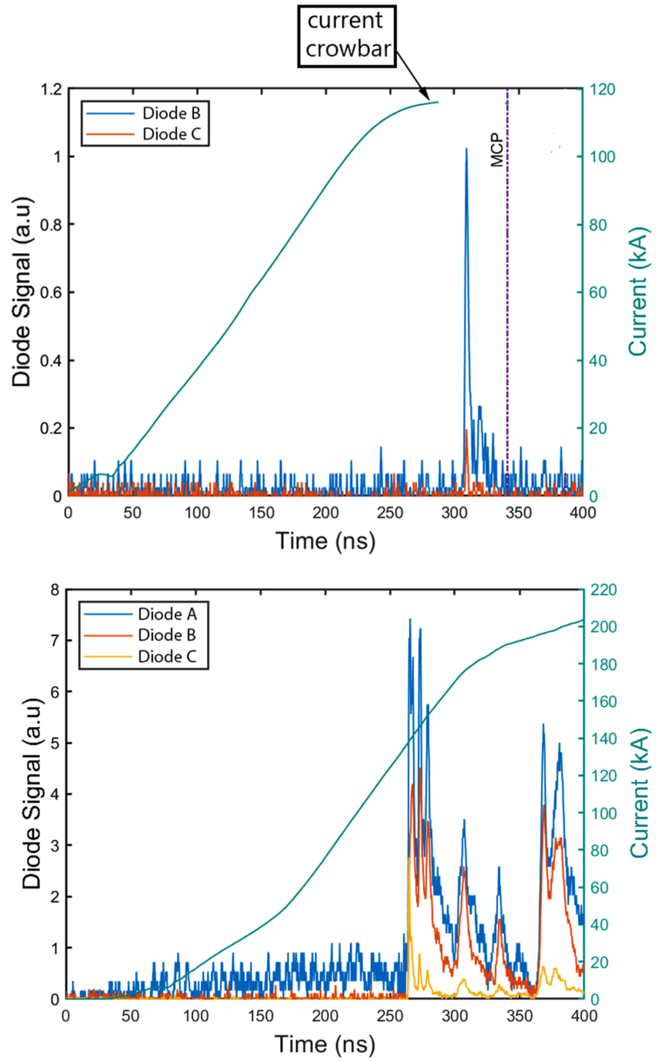

**FIG. 4.** Current traces and diode signals for two different shots. In both shots, Talbot–Lau fringe patterns are observed. A vertical line labeled "MCP" shows the timing of Fig. 3(a).

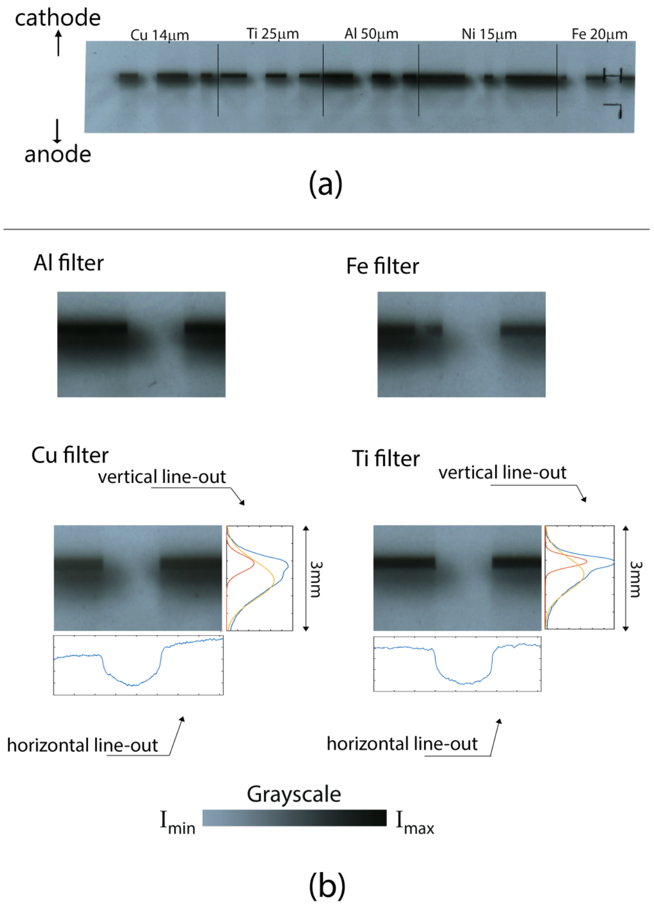

**FIG. 5.** (a) Raw slit-wire image (slit size ~30 $\mu$m) and (b) zoomed regions for specific filters blocked by 750 $\mu$m W wire diameter.

Besides this, the use of different filters in the slit-wire configuration demonstrates that the sources have different ranges of photon energy. Area-averaged lineouts of the exposed regions on both vertical and horizontal directions are included for the Cu and Ti filters. In the vertical direction, at least two sources separated by $(430 \pm 50)\,\mu$m can be fitted using Gaussian curves. On the other hand, in the horizontal direction, the shadows of the wires provide information of source size. Specific details on how source sizes are determined using slit-wire images can be found elsewhere.[27] The more pronounced source corresponds to a $(86 \pm 18)\,\mu$m size with emission in the 2–5 keV energy range as well as ~8 keV. The secondary source is larger than $750\,\mu$m in size with an emission concentrated in energies larger than 5 keV, reaching 9 keV or more. The upper limit cannot be properly determined using our current filter configuration. The origin of these sources is ascribed to the different mechanism of x-ray emission previously described. The smaller source is located in the crossing point of the X-pinch and it is attributed to hotspot formation and thermal x-ray emission. The second emission is ascribed to electron beams interacting with plasma on the anode side of the array [this asymmetric feature is also seen in Fig. 3(b)]

Despite the existence of (at least) two main sources of x-ray, the TXD images show Moire fringe formation under x-pinch illumination. In order to visualize the fringe shift produced by the deflectometry of x-rays in the material, schematic diagrams are shown in Fig. 6(a). The fringe shift is produced by the refraction due to gradients in the electron density $n_e$ of the x-ray beam.[9,34–36]

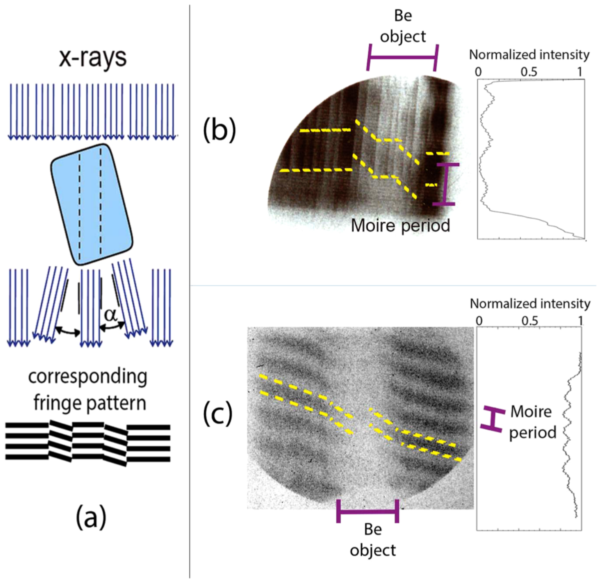

**FIG. 6.** (a) Schematic of angular refraction due to density gradients with a scheme of its fringe pattern. The x-rays are deviated by an angle α producing fringe shift. In (b) and (c), Talbot–Lau deflectometry fringe patterns are shown in yellow together with the lineouts of the raw images with (b) large and (c) short period. For visualization purposes, the contrast on the fringe patterns has been digitally enhanced.

The refraction angle $\alpha$ follows the relation

$$\alpha(x) = \frac{1}{n_c}\int_{-\infty}^{\infty} \frac{\partial\, n_e(x,y)}{\partial x}\, dy,$$

where $n_c$ is the critical electron density, which depends on the energy (wavelength) of the photons ($n_c = 4.56 \times 10^{28}$ cm$^{-3}$ for 8 keV photons). A shift in one fringe corresponds to the angular sensitivity of the TXD, which is 210 $\mu$rad in our scheme (as described in Sec. II). Further details on the TXD technique and the analysis of the deflectometer images have been published elsewhere.[9,34–36] Figure 6 also shows images taken with two different TXD systems from different shots: a large period fringe pattern with fringe shift due to refraction [Fig. 6(b)] and a small period fringe pattern [Fig. 6(c)]. These fringe patterns (large and small period) are used in order to test the deflectometer operation in our environment observing the same object with a different spatial resolution. Figure 6(b) has <14% of fringe contrast and an observable fringe shift corresponding to an electron density of $(7.13 \pm 0.44) \times 10^{23}$ cm$^{-3}$. The error bars in these measurements are derived from averaging the values obtained from refraction angles ($\alpha(x)$) measured (for each period on both sides of the object) as a function of the position ($x$) on the deflectometer image. This electron density corresponds to a Beryllium density of $(1.73 \pm 0.11)$ g/cm$^3$, a 6% difference with the tabulated value of 1.85 g/cm$^3$.[29] Similarly, in Fig. 6(c), the fluence of x-rays is enough to produce a Moire pattern with a fringe contrast above 8%. The fringe shift measured corresponds to an electron density of $(6.4 \pm 3.5) \times 10^{23}$ cm$^{-3}$, thus delivering a Beryllium density of $(1.56 \times 0.85)$ g/cm$^3$, i.e., a 15.7% difference with the tabulated value.

Even though the fringe contrast is lower than that measured using a standard medical x-ray tube and laser-driven x-ray backlighters, these results demonstrate the capability of the TXD diagnostic in pulsed power environments using an X-pinch as a backlighter source. The most likely reason for the reduced fringe contrast is the non-optimized x-ray source for 8 keV photons, since both filtered diodes and slit-wire images show the existence of (at least) two different sources each having wide energy spectra. Therefore, there are different Moire patterns superposed and recorded onto the x-ray film from photons of different energies in the spectral bandwidth allowed for the m = 1 Talbot order. This reduces the contrast of the final image. Additionally, noise and low flux also contribute to the reduced contrast from the theoretical value calculated.

An appropriate demonstration of the suitability of TXD diagnostics in pulsed power driver experiments must include additional analysis of mechanical and physical constrains. The gratings constituting the Talbot–Lau deflectometer are freestanding membranes meant for low energy photons, and, therefore, they are subject to damage in the harsh pulsed power environment. The most likely sources of damage come from heating and debris produced by the plasma discharge affecting mostly the grating closest to the backlighter ($g_0$). Both of these sources of damage are avoided by using an interchangeable protective filter in front of the $g_0$ grating.

Source grating survival was observed in all x-pinch shots. But, as shown in the post-shot images of Fig. 7, the protective aluminum filter can be severely damaged during the shot depending on

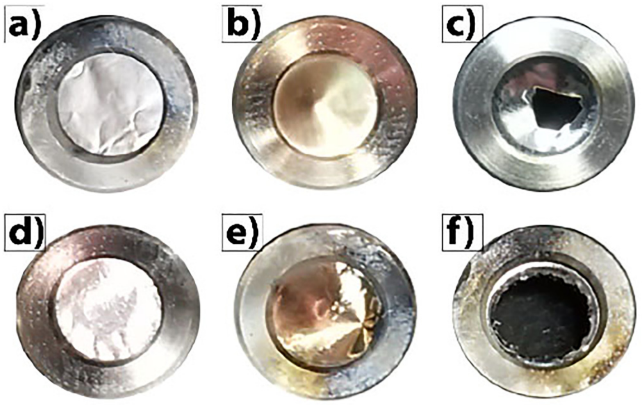

FIG. 7. Photographs of $g_0$ protective filters taken post shot. Signs of deposits are observed in every case. Signs of indentation in filters (b) and (c) with filter destruction in (c) and (f).

the maximum current achieved. These protective filters are located in front of the $g_0$ grating attached to a circular frame, which can be observed in this figure. These images seem to indicate that thicker filters would be better suited to protect the source grating from the x-pinch discharge. Even in the most extreme case where the protective foil was completely destroyed, the source grating survived the x-ray pulse only showing evidence of plasma deposition. There was no evidence of any structural modification or relevant morphological damages experienced by the gratings, supported by x-ray tube imaging performed *a posteriori*, where source grating performance matched previous results. Even if the grating experienced any expansion during the x-ray pulse (not expected from theoretical calculations),[6] this did not affect Moiré image acquisition, which was the goal when performing TXD using x-pinches as x-ray backlighters. Moreover, currents of ∼100 kA–1 MA are needed to drive an x-pinch configuration in order to produce an appropriate x-ray backlighter for pulsed power HED experiments. Notably, at our current level, the experimental results provide enough data to benchmark the use of TXD and grating survival for other pulsed power drivers of similar characteristics, where brighter (or optimized) X-pinches can be carried out as well as providing a starting point for future scaling experiments.

The performance of TXD in pulsed power environments can also be affected by the intense pulsed magnetic fields present, which is not necessarily the case for laser experiments. Intense pulsed magnetic fields can affect either the x-ray photons or the structure of the gratings. On the one hand, these fields might induce changes in the polarization of the x-ray photons. However, this effect is not detrimental in fringe formation produced by Moire deflectometry since it records the intensity of the light beam and not its phase (which is the case of interferometry). On the other hand, the fields can produce damage to the gratings in two different physics mechanisms: induced voltages in the grating membranes and magnetization of the deposited gratings.

Regarding induced voltages on the gratings, these might induce breakdown, which would destroy them during the pulsed discharge (not necessarily after the x-ray emission). Nevertheless, this mechanism requires that the normal component of the grating membranes has a non-zero component parallel with the magnetic field produced by the pulsed power driver. Therefore, careful consideration must be taken on the orientation of the gratings with respect to the pulsed magnetic field. In the implementation of the TXD system presented in this paper, the current flows through the central axis of the discharge (z-axis) producing the magnetic field in the azimuthal direction (θ-axis). In the x-pinch, x-ray emission is radially outward and, therefore, the orientation of the deflectometer is also in the radial direction (r-axis). Hence, no induced voltages on the gratings are expected on this particular configuration.

The magnetization of the gratings is an important issue if ferromagnetic materials are used in the lithographed membranes. If the fringes lithographed on the membranes get magnetized, they can attract one another by breaking the grating structure. As described in Sec. II, the membranes $g_0$ and $g_2$ use gold bars (diamagnetic). In contrast, $g_1$ uses nickel which is a ferromagnetic material whose magnetization saturates when the external magnetic field reaches approximately 0.3 T[30] which can be easily achieved in kA to MA generators. In the experiments, the $g_1$ component of the Talbot–Lau is located at ∼6 cm from the axis, where the magnetic field reaches a value of $B\ (\mathrm{T}) = 0.003\ I\ (\mathrm{kA})$. So, if the generator produces ∼1 kA/ns (the standard required for x-ray emission in X-pinches[14]), the $g_1$ component will saturate its magnetization before $t \sim 100$ ns which is before the x-ray emission from the X-pinch (as shown in Fig. 4). Therefore, the $g_1$ component is magnetized at saturation during the recording of the Talbot–Lau images shown in Fig. 6. Verification of the appropriate performance of the TXD system is also done by x-ray tube imaging performed *a posteriori*. All of these indicate that the present Talbot–Lau system can be confidently used in large current drivers (or higher current rate drivers) without the problem of breaking the ferromagnetic lithographed structures on the gratings.

## IV. CONCLUSIONS

The Talbot–Lau deflectometer has been adapted to be compatible with pulsed power experiments using an X-pinch source as a backlighter. It has been demonstrated that Moire fringe patterns and fringe shift due to refraction on a Beryllium object can be obtained even when the x-ray emission from the X-pinch is not optimized for our pulsed power driver parameters (in terms of the number of sources, source size, emission times, and photon fluence).

Nevertheless, the results shown in this paper emphasize the need for having some considerations when implementing the TXD technique in a pulsed power environment. In this regard, care must be taken with the use of interchangeable (or disposable) protective filters in front of the $g_0$ component in order to avoid any damage produced by plasma debris. In addition, the orientation of the gratings with respect to the global magnetic field should also be taken into account in order to avoid induced voltages. Nonetheless, it was demonstrated that the magnetization of the gratings is not an issue to consider in the TXD configuration presented here.

In order to improve the use of TXD diagnostics in pulsed power environments, further experiments are required to find an optimized X-pinch source. Different studies[12–23] have reached source sizes on the $\mu$m scale that would improve the spatial resolution of the diagnostic. This can also improve fringe contrast by optimizing the emission in the 8 keV range. In addition, the fringe contrast can be enhanced by tailoring the detection of the photons only where the TXD maximizes its contrast. This can be made by either choosing an adequate detector for photons (reducing the higher energy photon detection) such as an x-ray CCD or changing the Talbot order of the TXD (higher orders have narrow spectral bandwidths). With significantly more effort, a multi-layer mirror or crystal can be included in the system in order to obtain monochromatic emission, but this is beyond the scope of the present research.

Since visible probing of large pulsed power HED experiments where wires, foils, and/or magnetized liners is not possible due to high densities, the use of x-ray probing must be considered instead. However, in these cases, the $g_1$ and $g_2$ gratings should have a protection similar to the one used in the $g_0$ component, since these loads can be similarly destructive to these gratings than the X-pinch load is to $g_0$. The versatility of TXD allows its use to obtain high-resolution end-on or radial imaging of electron density mapping through dense plasma objects. These experiments will have variable electron densities and probably complex dense plasma structures as well. In order to avoid assumptions about the shapes or symmetries of these plasmas, each line-of-sight of the TXD technique will provide line-integrated density gradients instead, which can be deconvoluted using tomographic reconstruction of multiple line-of-sights. It is worth noting that TXD also delivers attenuation information and, moreover, it can provide elemental composition information through Z-average measurements,[35] which will deliver additional information for non-uniform densities along line-of-sight.

## ACKNOWLEDGMENTS

This work is supported by U.S. DoE/NNSA DE-NA0002955 grant and project Fondecyt/Regular No. 1171412. M. Vescovi acknowledges CONICYT-PFCHA/Magister Nacional/2018-22181702 grant for graduate studies.

## REFERENCES

[1] F. Pfeiffer, T. Weitkamp, O. Bunk, and C. David, Nat. Phys. **2**, 258 (2006).

[2] T. Weitkamp, A. Diaz, C. David, F. Pfeiffer, M. Stampanoni, P. Cloetens, and E. Ziegler, Opt. Express **13**, 6296 (2005).

[3] Y. Takeda, W. Yashiro, T. Hattori, A. Takeuchi, Y. Suzuki, and A. Momose, Appl. Phys. Express **1**, 1170021 (2008).

[4] L. B. Da Silva, T. W. Barbee, R. Cauble, P. Celliers, D. Ciarlo, S. Libby, R. A. London, D. Matthews, S. Mrowka, C. Moreno, D. Ress, J. E. Trebes, A. S. Wan, and F. Weber, Phys. Rev. Lett. **74**, 3991 (1995).

[5] S. Zhou and A. Brahme, Phys. Med. **24**, 129 (2008).

[6] M. P. Valdivia, D. Stutman, C. Stoeckl, W. Theobald, C. Mileham, I. A. Begishev, J. Bromage, and S. P. Regan, Rev. Sci. Instrum. **87**, 023505 (2016).

[7] M. P. Valdivia, D. Stutman, C. Stoeckl, C. Mileham, I. A. Begishev, W. Theobald, J. Bromage, S. P. Regan, S. R. Klein, G. Muñoz-Cordovez, M. Vescovi, V. Valenzuela-Villaseca, and F. Veloso, Rev. Sci. Instrum. **87**, 11D501 (2016).

[8] M. R. Gomez *et al.*, Phys. Rev. Lett. **113**, 155003 (2014).

[9] M. P. Valdivia, D. Stutman, and M. Finkenthal, Rev. Sci. Instrum. **85**, 073702 (2014).

[10] S. M. Zakharov, G. V. Ivanenkov, A. A. Kolomenskii, S. A. Pikuz, A. I. Samokhin, and I. Ulshmid, Sov. Tech. Phys. Lett. **8**, 456 (1982).

[11] S. M. Zakharov, G. V. Ivanenkov, A. A. Kolomenskii, S. A. Pikuz, A. I. Samokhin, and I. Ulshmid, Sov. J. Plasma Phys. **13**, 115 (1987).

[12] T. A. Shelkovenko, D. B. Sinars, S. A. Pikuz, K. M. Chandler, and D. A. Hammer, Rev. Sci. Instrum. **72**, 667 (2001).

[13] T. A. Shelkovenko, D. B. Sinars, S. A. Pikuz, and D. A. Hammer, Phys. Plasmas **8**, 1305 (2001).

[14] S. A. Pikuz, T. A. Shelkovenko, and D. A. Hammer, Plasma Phys. Rep. **41**, 445 (2015).

[15] M. Haines, Plasma Phys. Control Fusion **53**, 93001 (2011).

[16] D. H. Kalantar and D. A. Hammer, Rev. Sci. Instrum. **66**, 779 (1995).

[17] S. A. Pikuz, T. A. Shelkovenko, and V. M. Romanova, Rev. Sci. Instrum. **68**, 740 (1997).

[18] S. V. Lebedev, F. N. Beg, S. N. Bland, J. P. Chittenden, A. E. Dangor, M. G. Haines, and M. Zakaullah, Rev. Sci. Instrum. **72**, 671 (2001).

[19] T. A. Shelkovenko, S. A. Pikuz, and D. A. Hammer, Plasma Phys. Rep. **42**, 226 (2016).

[20] F. N. Beg, R. Stephens, E. Shiptin, D. Haas, G. Andreev, S. Eddinger, and H. Haung, AIP Conf. Proc. **808**, 125 (2006).

[21] F. N. Beg, R. B. Stephens, H.-W. Xu, D. Haas, S. Eddinger, G. Tynan, E. Shipton, B. DeBono, and K. Wagshal, Appl. Phys. Lett. **89**, 101502 (2006).

[22] D. A. Hammer, D. H. Kalantar, K. C. Mittal, and N. Qi, Appl. Phys. Lett. **57**, 2083 (1990).

[23] T. A. Shelkovenko, S. A. Pikuz, C. L. Hoyt, A. D. Cahill, and D. A. Hammer, IEEE Trans Plasma Sci. **42**, 748 (2014).

[24] S. H. Glenzer *et al.*, Science **327**, 1228 (2010).

[25] T. Weitkamp, Proc. SPIE **5536**, 181 (2004).

[26] H. Chuaqui, E. Wyndham, C. Friedli, and M. Favre, Laser Part. Beams **15**, 241 (1997).

[27] P. Choi, C. Dumitrescu, E. Wyndham, M. Favre, and H. Chuaqui, Rev. Sci. Instrum. **73**, 2276 (2002).

[28] S. N. Bland, D. J. Ampleford, S. C. Bott, S. V. Lebedev, J. B. A. Palmer, S. A. Pikuz, and T. A. Shelkovenko, Rev. Sci. Instrum. **75**, 3941 (2004).

[29] G. W. C. Kaye and T. H. Laby "Properties of the elements," in Tables of Physical & Chemical Constants, 16th ed. (online version 1.0, 2005); see www.kayelaby.npl.co.uk.

[30] M. Hanson and C. Johansson, in *Magnetic Hysteresis in Novel Magnetic Materials*, edited by G. C. Hadjipanayis (Kluwer Academic Publishers, 1997), pp. 499–503.

[31] M. Engelhardt, C. Kottler, O. Bunk, C. David, C. Schroer, J. Baumann, M. Schuster, and F. Pfeiffer, J. Microsc. **232**, 145–157 (2008).

[32] B. L. Henke, E. M. Gullikson, and J. C. Davis, At. Data Nucl. Data Tables **54**, 181 (1993).

[33] AXUV family detectors developed by Opto Diode Corporation, California USA; see http://www.optodiode.com/.

[34] M. P. Valdivia, D. Stutman, and M. Finkenthal, J. Appl. Phys. **114**, 163302 (2013).

[35] M. P. Valdivia, D. Stutman, and M. Finkenthal, Appl. Opt. **54**, 2577 (2015).

[36] M. P. Valdivia, D. Stutman, C. Stoeckl, C. Mileham, J. Zou, S. Muller, K. Kaiser, C. Sorce, P. A. Keiter, J. R. Fein, M. Trantham, R. P. Drake, and S. P. Regan, Rev. Sci. Instrum. **91**, 023511 (2020).

[37] R. P. Drake, *High Energy Density Physics: Fundamentals, Inertial Fusion and Experimental Astrophysics* (Springer-Verlag, 2006).

[38] R. P. Drake, Phys. Plasmas **16**, 055501 (2009).

[39] M. K. Matzen *et al.*, Phys. Plasmas **12**, 055503 (2005).